JACS
JOURNAL OF THE AMERICAN CHEMICAL SOCIETY
Article
pubs.acs.org/JACS

Unravelling Li-Ion Transport from Picoseconds to Seconds: Bulk versus Interfaces in an Argyrodite Li_6PS_5Cl–Li_2S All-Solid-State Li-Ion Battery

Chuang Yu,[†] Swapna Ganapathy,[†] Niek J. J. de Klerk,[†] Irek Roslon,[†] Ernst R. H. van Eck,[‡] Arno P. M. Kentgens,[‡] and Marnix Wagemaker*[,†]

[†]Department of Radiation Science and Technology, Delft University of Technology, Mekelweg 15, Delft 2629 JB, The Netherlands
[‡]Institute for Molecules and Materials, Radboud University Nijmegen, Heyendaalseweg 135, Nijmegen 6525 AJ, The Netherlands

Supporting Information

ABSTRACT: One of the main challenges of all-solid-state Li-ion batteries is the restricted power density due to the poor Li-ion transport between the electrodes via the electrolyte. However, to establish what diffusional process is the bottleneck for Li-ion transport requires the ability to distinguish the various processes. The present work investigates the Li-ion diffusion in argyrodite Li_6PS_5Cl, a promising electrolyte based on its high Li-ion conductivity, using a combination of ^{7}Li NMR experiments and DFT based molecular dynamics simulations. This allows us to distinguish the local Li-ion mobility from the long-range Li-ion motional process, quantifying both and giving a coherent and consistent picture of the bulk diffusion in Li_6PS_5Cl. NMR exchange experiments are used to unambiguously characterize Li-ion transport over the solid electrolyte–electrode interface for the electrolyte–electrode combination Li_6PS_5Cl–Li_2S, giving unprecedented and direct quantitative insight into the impact of the interface on Li-ion charge transport in all-solid-state batteries. The limited Li-ion transport over the Li_6PS_5Cl–Li_2S interface, orders of magnitude smaller compared with that in the bulk Li_6PS_5Cl, appears to be the bottleneck for the performance of the Li_6PS_5Cl–Li_2S battery, quantifying one of the major challenges toward improved performance of all-solid-state batteries.

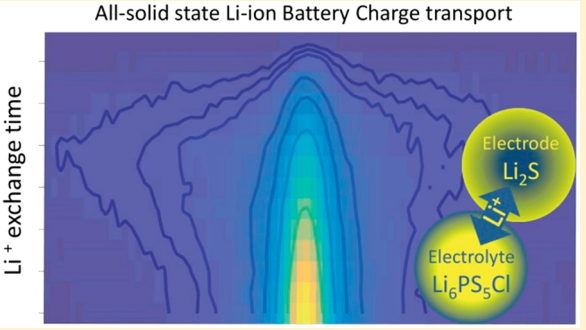

INTRODUCTION

The demand for safe electrical energy storage technologies with high energy density for electric vehicle applications is rapidly increasing.[1] All-solid-state Li-ion batteries are appealing because of the inherent improvement of battery safety associated with replacing the flammable organic electrolyte in Li-ion batteries.[2−9] This has the additional advantage of less stringent packaging demands, potentially leading to higher energy densities and allowing more design freedom.[2,3,6,8] The challenge is to develop solid electrolyte materials that combine a high conductivity with a large chemical and electrochemical stability.[2−6,9,10] Current liquid electrolytes have conductivities around 10^{-2} S/cm with a transference number close to 0.5. For solid electrolytes having a transference number close to unity means that bulk conductivity between 10^{-2} and 10^{-3} S/cm is required. In addition to a high electrolyte conductivity, another prerequisite is a facile charge transfer reaction of the Li-ion over the electrolyte–electrode interface.[10] Compared with the solid–liquid electrode–electrolyte interface in Li-ion batteries, this poses a considerable challenge, not only due to potential chemical and electrochemical instabilities but also because it requires the establishment of good contact and maintaining this during the volumetric changes of the electrode materials upon battery cycling. In addition, space charges driven by the potential difference between the positive electrode and electrolyte may lead to local Li-ion depletion of the electrolyte, posing an additional hurdle for Li-ion transport over the solid–solid electrode–electrolyte interface.[6,11,12]

Intensive research efforts have led to several families of excellent solid Li-ion conductors including the sulfides (Li_2S–P_2S_5, Li_2S–SiS_2, Li_2S–GeS_2),[13−15] oxides ($Li_7La_3Zr_2O_{12}$ and $Li_{3x}La_{2/3-3x}TiO_3$),[16] and phosphates (LiPON, $Li_{1+x}Al_xGe_{2-x}(PO_4)_3$, $Li_{1+x}Ti_{2-x}Al_x(PO_4)_3$).[3,4,9,17] Generally, the chemically stable oxides and phosphates display relatively low ionic conductivity and high grain boundary resistances.[4] Sulfides generally offer higher conductivities,[10] and their relative low melting temperatures compared with the oxides and phosphates apparently leads to a relatively low grain boundary resistance.[6,9,18] The downside of the sulfide solid electrolytes is their sensitivity to air. However, replacing S with Se has been shown to improve their chemical stability.[19,20] An important family of sulfide solid electrolytes are the Li-argyrodites, Li_6PS_5X (X = Cl, Br, and I) providing Li-ion conductivities in the range of 10^{-2} to 10^{-3} S/cm at room temperature.[15] The conductivities of these materials are slightly smaller compared

Received: May 17, 2016
Published: August 11, 2016

DOI: 10.1021/jacs.6b05066
J. Am. Chem. Soc. 2016, 138, 11192−11201

with $Li_{10}GeP_2S_{12}$; however their much cheaper precursors make this family of materials attractive for the application in all-solid-state batteries. In addition to the high Li-ion conductivities, Li_6PS_5Cl is reported to have a wide electrochemical window of up to 7.0 V vs Li/Li^+.[21] Boulineau et al.[21,22] assembled solid-state cells using Li_6PS_5Cl as the electrolyte, $LiCoO_2$ as the cathode, and spinel $Li_4Ti_5O_{12}$ as the anode, exhibiting excellent electrochemical performance. Chen and Adams[23] combined sulfur as electrode material with Li_6PS_5Br to construct a solid-state cell, also showing excellent performance with an initial discharge capacity of 1355 mAh/g and reversible capacity of 1080 mAh/g after 50 cycles. The excellent electrochemical performance of the solid-state battery was attributed to the small particle size of the active materials. Rao et al.[24] reported the synthesis protocols for argyrodite Li_6PS_5X (X = Cl, Br, I) using high mechanical milling speeds resulting in a room temperature conductivity on the order of 10^{-3} S/cm. Additionally using neutron powder diffraction during annealing, Rao et al.[25] were able to establish a clear correlation between the disorder in the S^{2-}/Cl^- or S^{2-}/Br^- distribution and the conductivity, which was also supported by recent bond-valence analysis.[19] In Li_6PS_5Cl, Li-ion mobility occurs at different time- and length-scales where three types of transitions were distinguished based on calculations in the argyrodite structure,[19,26] all three of which are necessary for the macroscopic conductivity. For two of these transitions, activation energies in the range of 0−0.2 eV were predicted, while the transition, which limits the macroscopic conductivity, was predicted to have an activation energy close to 0.3 eV. Based on this, the initially reported fast Li-ion diffusion probed by ^{7}Li NMR appears to be due to a local diffusion process.[19,27] Confusingly, activation energies of the macroscopic conductivity, measured by impedance spectroscopy, are reported to be very small at 0.11 eV, as well as very large up to 0.56 eV.[15,21,24−28] This makes it very difficult to gain insight into the various diffusion processes in Li_6PS_5Cl, and their role in the performance of all-solid-state batteries.

An important experimental challenge is to unravel the different Li-ion diffusion processes, ranging from short-range vibrations at time scales on the order of 10^{-13} s to transport over grain boundaries and electrode interfaces taking place at a time scale potentially reaching seconds. Using impedance spectroscopy, it is not trivial to establish the bulk Li-ion conductivity and underlying diffusion mechanism due to the influence of porosity, grain boundaries, and effects introduced by the electrodes in contact with the solid electrolyte under investigation. An even greater challenge is to separate the influence of grain boundaries that need to be crossed from one solid electrolyte grain to the other, and the charge transfer reaction over the electrolyte−electrode interface from the bulk conductivity. This is however essential information to gain direct insight in the bottleneck for Li-ion transport, one of the major limitations of all-solid-state batteries, which would potentially give a pivotal direction toward improved power performance of all-solid-state batteries. In this context nuclear magnetic resonance (NMR) spectroscopy offers unique complementary information to impedance spectroscopy, offering high sensitivity to the atomic mobility of the ^{7}Li nucleus and being a nondestructive contactless probe in battery materials.[29−32] The value of NMR spectroscopy for solid electrolyte battery research is demonstrated by recent research giving quantitative and mechanistic insight in the Li-ion and Na-ion bulk mobility mechanism due to the large dynamic range that can be probed.[20,33,34] An additional opportunity of solid-state NMR in multiphase battery materials, consisting of either multiple electrode phases or a mixture of electrode and electrolyte phases, is the ability to probe the spontaneous Li-ion exchange between different phases, giving unique selectivity for charge transfer over phase boundaries.[35,36]

In the present work, we aim at a detailed understanding of the conductivity in the argyrodite Li_6PS_5Cl solid electrolyte by distinguishing local Li-ion mobility, bulk diffusion, the impact of grain boundaries, and the charge transfer kinetics over the interface with the Li_2S electrode. This combination of materials is shown to maintain capacities above 300 mAh/g for 40 cycles. Understanding of the bulk diffusion mechanism is achieved by detailed comparison of NMR spin−lattice relaxation experiments with molecular dynamics (MD) simulations based on density functional theory (DFT). Comparison with the room temperature conductivity based on impedance spectroscopy gives insight into the role of solid electrolyte grain boundaries. Moreover, NMR exchange spectroscopy is used to probe the Li-ion transport over the interface between the Li_6PS_5Cl solid electrolyte and the Li_2S positive electrode, giving unique insight into the charge transfer reaction, which appears vital for the power performance of all-solid-state batteries.

EXPERIMENTAL SECTION

Reagent-grade Li_2S (99.98%, Sigma-Aldrich), P_2S_5 (99%, Sigma-Aldrich), and LiCl (99.0%, Sigma-Aldrich) crystalline powders were used as starting materials. The required amounts of starting materials, according to the molar ratios of stoichiometric Li_6PS_5Cl, were ball milled in a WC coated (inner) stainless steel jar with 10 WC balls (8 g/ball) filled in an argon filled glovebox (H_2O, O_2 < 0.3 ppm) to prevent reactions with oxygen and moisture. The total weight of the mixture was almost 2.0 g, the ball milling rotation speed was fixed at 550 rpm, and different milling durations were applied. After various milling times, the jar was transferred to the glovebox and an amount of powder was collected to perform powder XRD. After the ball milling process, the mixture was sealed in a quartz tube and annealed at 550 °C for 5 h to obtain the final Li_6PS_5Cl solid electrolyte.

Powder XRD patterns were collected over a 2θ range of 10−160° 2θ to identify the crystalline phases of the prepared materials using Cu Kα X-rays (1.5406 Å at 45 kV and 40 mA) on an X'Pert Pro X-ray diffractometer (PANalytical). To prevent reaction with moisture and oxygen, the powder materials were sealed in an airtight XRD sample holder in an argon filled glovebox.

Ionic conductivities of the ball-milled powder and the final Li_6PS_5Cl solid electrolyte were measured by pelletizing the powder applying a diameter of 10 mm. Stainless-steel disks were attached on both faces of the pellets, and AC impedance measurements were performed for the cell with an Autolab (PGSTAT302N) in the frequency range of 0.1 Hz to 1 MHz with an applied voltage of 0.05 V.

Solid-state NMR measurements were performed on a Chemagnetics 400 Infinity spectrometer (B_0 = 9.4 T), operating at a ^{7}Li resonance frequency of 155.506 MHz. The $\pi/2$ pulse length was determined to be 3.1 μs with an RF field strength of 85 kHz. Chemical shifts were referenced with respect to a 0.1 M LiCl solution. The Li_2S electrode−Li_6PS_5Cl solid electrolyte mixture used for one-dimensional (1D) ^{7}Li NMR exchange experiments were prepared by mixing the ball milled Li_2S (500 rpm, 3 h) and the ball-milled Li_6PS_5Cl (450 rpm, 6 h) with a rotation speed of 400 rpm for 3 h based on the weight ratio. The air sensitive Li_6PS_5Cl solid electrolyte sample and the Li_2S electrode−Li_6PS_5Cl solid electrolyte mixture were sealed in custom-made Teflon tubes in an argon filled glovebox (H_2O, O_2 < 0.3 ppm). Variable temperature measurements were performed using a 5 mm static goniometer probe. For the Li_6PS_5Cl sample, a temperature range of −120 to +180 °C was probed. T_1 relaxation times were determined at various temperatures using a saturation recovery experiment. Corresponding $T_{1\rho}$ measurements were performed using the spin-

DOI: 10.1021/jacs.6b05066
J. Am. Chem. Soc. 2016, 138, 11192−11201

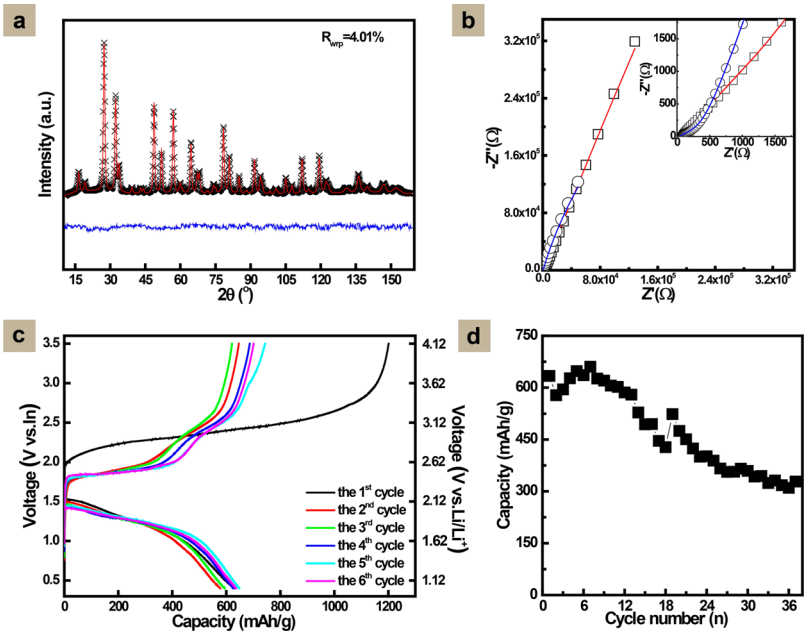

Figure 1. (a) XRD refinement of the prepared Li_6PS_5Cl material. (b) Room temperature impedance spectroscopy of the prepared Li_6PS_5Cl materials. The open square and circle symbols represent the impedance of the ball milled and annealed material, respectively, and the solid lines represent fits using an equivalent circuit $(R_1Q_1)(R_2Q_2)Q_3$. (c) Galvanostatic voltage curves during the first six cycles of the assembled $Li_2S/Li_6PS_5Cl/In$ solid-state battery at a current density of 0.064 mA/cm^2 applied between 0.4 and 3.5 V vs In (1.02−4.12 V vs Li^+/Li). (d) Capacity upon cycling of the solid-state battery.

lock method at three different lock frequencies, $\omega_1/(2\pi) \approx 11$, 42, and 84 kHz, respectively. Additional single pulse experiments were performed at different temperatures to determine the evolution of line width as a function of temperature employing a spectral width of 50 kHz. In each case, a recycle delay of $3T_1$ was used. For the mixture, additional one-dimensional (1D) exchange experiments were performed at temperatures ranging from 213 to 323 K. The pulse sequence used has been described in detail elsewhere with the appropriate phase cycle for cancellation of direct magnetization that may occur after T_1 relaxation.[35,36] Briefly the sequence consists of $\pi/2$, τ, π, τ, $-\pi/2$, t_{mix}, $+\pi/2$, acquisition. An echo time τ ranging from 200 to 400 μs was utilized so as to preserve the intensity of the narrow Li_6PS_5Cl resonance and filter out the broad Li_2S resonance, effectively functioning as a T_2 filter. These 1D exchange experiments were performed for a range of mixing times, t_{mix}, to follow the spontaneous equilibrium exchange of Li between the Li_6PS_5Cl and Li_2S phases

Laboratory-scale solid-state $Li_2S/Li_6PS_5Cl/Li$−In batteries were fabricated. Commercial Li_2S was first milled with a rotation speed of 500 rpm for 3 h and then milled with Li_6PS_5Cl and super P (TIMCAL) with a weight ratio of 4:4:2 using a rotation speed of 400 rpm for 3 h to obtain the final cathode mixture. Analysis of the particle size broadening from the refined XRD patterns resulted in electrolyte and electrode particle sizes of approximately 7 and 32 nm, respectively. A two-layer pellet, 10 mm in diameter, consisting of 12 mg of the described cathode mixture and 88 mg of Li_6PS_5Cl solid electrolyte, was obtained by pressing the powder electrode and electrolyte together under 6 tons. After that, a piece of In alloy foil was attached to the other side. Subsequently the full solid-state battery pellet was pressed under 2 tons for 30 s. The assembled cell was charged and discharged by applying a current density of 0.064 mA/cm^2 between 0.4 and 3.5 V vs In to evaluate the electrochemical performances. The obtained capacity was normalized by the weight of Li_2S in the cathode electrode. Cyclic voltammetry (CV) measurements of the solid-state battery were performed at different voltage windows applying a sweep speed of 0.5 mV/s. Electrochemical impedance spectroscopy measurements were conducted on an Autolab PGSTAT302N before and after the electrochemical cycling process in the frequency range of 0.1 Hz and 1 MHz with an applied voltage of 0.05 V.

DFT MD simulations were performed using the GGA approach, with the PAW−PBE basis set as implemented in VASP.[37] A single unit cell was used, for the minimizations, a k-point mesh of 2 × 2 × 2 was used, and for the MD simulations, a k-point mesh of 1 × 1 × 1 was used. The lattice parameters after minimization differed by less as 2% from the experimental value. During the MD simulations a time of 100 ps was simulated, with time steps of 2 fs; the time allowed for equilibration was 2.5 ps. The jump frequencies were determined using the same approach as described by de Klerk and Wagemaker.[38]

RESULTS AND DISCUSSION

Synthesis, Impedance Spectroscopy, and Electrochemical Performance. In the present synthesis, 16 h of ball milling at 550 rpm followed by annealing at 550 °C for 5 h results in the argyrodite cubic structure (space group $F\bar{4}3m$), as confirmed by the Rietveld refinement of the XRD data in Figure 1a, resulting in a lattice parameter of 9.8290 Å and comparable S/Cl disorder as reported by Rao and Adams[24] and Kress and Hafner.[37] Room temperature impedance spectroscopy, shown in Figure 1b, indicates a conductivity of $(1.18 \pm 0.04) \times 10^{-3}$ S/cm for the prepared Li_6PS_5Cl material, a value similar to that reported by Boulineau et al.,[21] and Rao and Adams[24] and Kress and Hafner.[37] The refinement results of the impedance spectra are shown in Table S1 in the Supporting Information.

Tatsumisago et al. used Li_2S as positive electrode material in combination with $80Li_2S$−$20P_2S_5$, suggesting that reducing the particle size of the Li_2S active material and of the Li_2S−C composite are two important factors to improve the capacity of Li_2S all solid-state cells.[5] Following a similar strategy, Chen and Adams[23] combined the S cathode with Li_6PS_5Br to construct a solid-state cell, also showing excellent performance with an initial discharge capacity of 1355 mAh/g and reversible capacity of 1080 mAh/g after 50 cycles. In the present work, an all-solid-state battery is assembled combining the Li_6PS_5Cl electrolyte with a nanostructured Li_2S−C composite as positive electrode

DOI: 10.1021/jacs.6b05066
J. Am. Chem. Soc. 2016, 138, 11192−11201

material and indium as negative electrode material, as described in the Experimental Section. Cyclic voltammetry was performed applying various voltage windows, resulting in an optimal performance between 0.4 and 3.5 V vs In (1.0 to 4.1 V vs Li/Li^+), see Figure S1 in the Supporting Information. Galvanostatic cycling was performed applying the optimal voltage cut-offs at a constant current density of 0.064 mA/cm^2 at 298 K. The charge/discharge curves and the corresponding capacity retention upon cycling are shown in Figure 1c,d, respectively. The cell capacity is reported as the capacity per gram of Li_2S resulting in an initial charge and discharge capacity of approximately 1200 and 634 mAh/g corresponding to a Coulombic efficiency of only 52.8%. The low Coulombic efficiency during the first few cycles may be a result of the large volume changes associated with the Li_2S positive electrode, where the volume decrease during oxidation may cause loss of contact of the Li_xS phases with the solid electrolyte or the carbon electronic conducting phase making subsequent reduction impossible. The initial cycle displays only one charge plateau around 2.4 V and one discharge plateau at 1.5 V vs In. During subsequent cycling, two charge plateaus at 1.8 and 2.4 V vs In, and one discharge plateau at 1.5 V vs In are observed. In contrast, using the same electrode combination and applying Li_3PO_4–Li_2S–SiS_2 as solid electrolyte resulted in a single charge plateau at 2.0 V and a discharge plateau at 1.5 V vs In upon cycling.[39] The present voltage curves appear more like cells applying an organic liquid electrolyte in combination with the Li_2S–C positive electrode, which also display two charge plateaus, at 2.40 and 2.04 V vs Li/Li^+,[40] close to the presently observed values.

The cycling capacity in Figure 1d shows that the cell delivers a capacity of 636 mAh/g after 6 cycles, a relatively good capacity retention compared with previously reported all-solid-state batteries applying Li_2S as a positive electrode.[39,41−43] Possible explanations for the relatively good electrochemical performance of the present $Li_2S/Li_6PS_5Cl/In$ cell are the optimized voltage window, small particle sizes of electrode and electrolyte, and better performance of the Li_6PS_5Cl solid electrolyte.[5] To monitor the internal resistance of the battery electrochemical impedance spectroscopy (EIS) was performed on the cell before and after cycling, shown in the Supporting Information Figure S2. For the fresh cell, the impedance spectrum displays a resistance of 111 ± 2 Ω at high frequencies and an interface resistance of less than 300 ± 70 Ω. However, after 30 and 37 cycles, both impedance spectra indicate two intersections with the horizontal axis in the high frequencies (left, R_1) and low frequencies (right, R_2). R_1 reflects the resistance of the solid electrolyte, resulting in 144 ± 1 and 176 ± 2 Ω after 30 and 37 cycles, respectively, only a slight increase compared with the fresh cell, indicating that the charge resistance of Li-ions in Li_6PS_5Cl does not increase significantly upon cycling. $(R_2 - R_1)$ is suggested to reflect the interface resistance[44] of the Li_2S electrode with the Li_6PS_5Cl solid electrolyte, resulting in 1930 ± 41 Ω and 3980 ± 54 Ω after 30 and 37 cycles, respectively. This indicates a significant growth of the interfacial resistance upon cycling, potentially responsible for the observed capacity fading.

Li_6PS_5Cl Bulk Li-Ion mobility by Molecular Dynamics and 1D NMR Spin–Lattice Relaxation. The Li-density and transitions between Li-sites from the DFT MD simulations of Li_6PS_5Cl at three different temperatures are shown in Figure 2. In the Li_6PS_5Cl crystalline lattice, the Li-ions occupy tetrahedral positions (Wyckoff notation 48h). The duration of the DFT

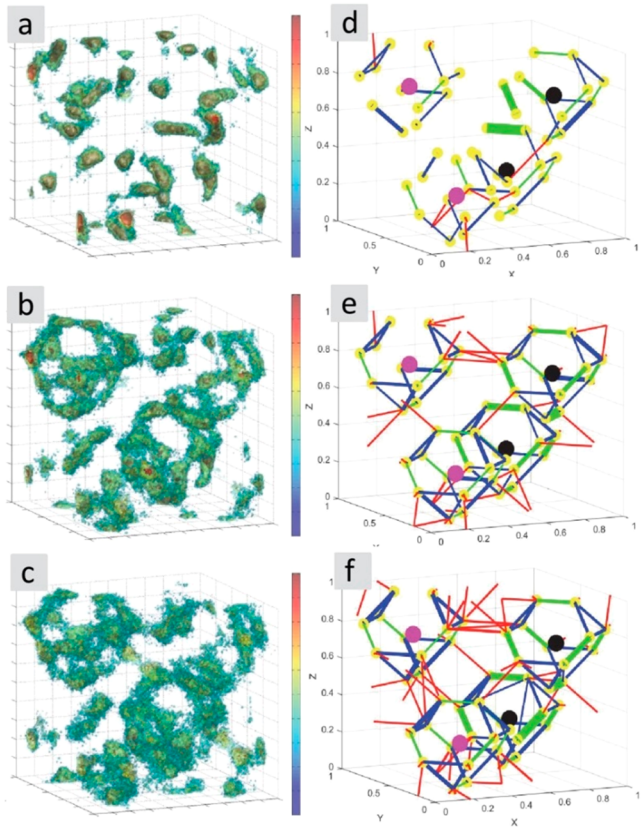

Figure 2. (a–c) The integrated Li density of the MD simulations in Li_6PS_5Cl at (a) 300, (b) 450, and (c) 600 K. (d–f) Jump statistics from the MD simulations at (d) 300, (e) 450, and (f) 600 K. The lines represent three types of Li-ion transitions; (green) back and forth jumps between 48h-sites; (blue) transitions within the cage consisting of 48h sites; (red) intercage jumps. The thickness of the green, blue, and red lines indicates the frequency of the transitions. Yellow spheres indicate 48h-sites for Li, black spheres indicate the S atoms, and purple spheres indicate the Cl atoms.

MD simulations are restricted to 10^{-10} s because of the extensive computational time required for these calculations. At 300 K, the Li-density mainly displays local Li-ion mobility over the duration of the MD simulations, as indicated by the unconnected regions of high Li-ion density in Figure 2a. At this temperature, the Li-ion dynamics is dominated by back-and-forth transitions between neighboring sites (1.68 Å apart), which does not lead to macroscopic Li-ion conductivity. At 450 K, the Li-density (Figure 2b) reflects the cage structure formed by the Li-ion (48h) sites around a central S or Cl atom. At this temperature, the dominant diffusion is within the cages, referred to as intracage diffusion, also not leading to macroscopic conductivity. Only very occasionally do Li-ions make the transition between neighboring cages (during the 10^{-10} s simulation). Thereby three types of transitions can be distinguished from the MD simulations, short-range back-and-forth (48h–48h) transitions, short-range intracage transitions, and long-range intercage transitions. Since all three types of transition are required to make macroscopic conductivity in Li_6PS_5Cl possible, the intercage transition is shown to be the rate-limiting process. In Figure 2d–f for each of these three processes the transition frequency, determined from the MD simulations, is schematically represented by the thickness of the line connecting the starting and end points of the Li-ion jumps

DOI: 10.1021/jacs.6b05066
J. Am. Chem. Soc. 2016, 138, 11192–11201

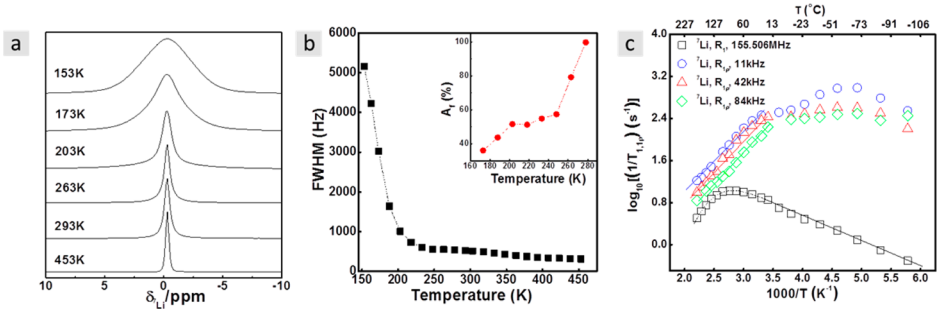

Figure 3. (a) Motional narrowing curves of the static ^{7}Li NMR resonance of Li_6PS_5Cl. (b) Evolution of the fwhm of the static ^{7}Li NMR resonance of Li_6PS_5Cl with temperature. The inset shows the temperature dependence of the fraction of fast lithium ions (A_f) calculated by integrating the area of the fitted line shape (as described in the text). (c) Arrhenius plots of the ^{7}Li spin−lattice relaxation (SLR) NMR rates measured in both the laboratory (R_1) and the rotating ($R_{1\rho}$) frame of reference. The Larmor frequency is 155.506 MHz and the locking frequencies are 11, 42, and 84 kHz, respectively.

in the unit cell. In Figure 2d−f, it is clearly observed that increasing the temperature leads to a rise in the number of intercage transitions, thus increasing macroscopic diffusion. The present study does not show transitions involving those other than type 5 tetrahedral sites,[26,27] which are localized in the common faces of face sharing double tetrahedra and form the cage like structure (built up by 12 type 5 positions) centered by either a S or Cl atom. The absence of the other type of sites in the diffusion pathway may be a consequence of the relatively short calculation time. However, it does indicate that the present DFT based MD simulations predict that the type 5 sites dominate the diffusion mechanism. Also the suggested transition site connecting the cages, type 2, having common edges of neighboring tetrahedra, is not specifically observed during the intercage transition, as illustrated by the various possible intercage transitions at 600 K (Figure 2).

From the intercage jump frequencies predicted by the MD simulations, the conductivity can be calculated via a combination of the Einstein−Smoluchowski relation and the Nernst−Einstein equation[45] assuming no correlation effects,[46] which is a reasonable assumption given the relatively low amount of vacancies. The transition frequencies, resulting diffusion coefficients, and conductivities are given in Table S2 in the Supporting Information, and the conductivities are shown in Figure 5. At 450 and 600 K, this results in a conductivity due to the intracage transitions of 2.6 ± 1.0 and 4.7 ± 0.7 S/cm, respectively. Transition state theory can be used to calculate the activation energy of the transitions, ΔE_a, from the jump frequencies according to[47] $\Delta E_a = -kT \ln(\nu/\nu_0)$ where k is Boltzmann's constant, T the temperature in Kelvin, and ν_0 the attempt frequency, which is assumed to be $\nu_0 = 10^{13}$ Hz.[48] The results in Supporting Information Table S2 show that the two local transitions, back-and-forth jumps and intracage jumps, have similar activation energies, between 0.10 and 0.17 eV (depending on temperature), whereas the intercage jumps have a significantly larger activation energy of 0.23−0.25 eV (depending on temperature).

Using a bond valence approach in a broad range of argyrodite compositions, Chen et al.[19] also distinguished the two types of local transitions from the intercage transitions for Li_6PS_5Cl resulting in activation energies of 0.15, 0.18, and 0.22 eV, in good agreement with the present values based on DFT MD simulations.

Solid-state ^{7}Li NMR experiments are used to probe the bulk mobility of the Li-ions in Li_6PS_5Cl, which in combination with the MD simulations gives insight in the Li-ion diffusion mechanism. The high mobility of the Li-ions in the Li_6PS_5Cl lattice is reflected by the so-called "motional" narrowing of the static ^{7}Li NMR spectra with increasing temperature in Figure 3a, similar to what was observed by Deiseroth et al.[15] At the lowest temperature, 153 K, the spectrum can be fitted by a broad Gaussian where the width is dominated by the dipolar coupling between the spins of the ^{7}Li nuclei. Above 153 K, the static ^{7}Li NMR resonance becomes narrower, because the mobile Li-ions are increasingly able to average out the dipolar interactions. This can be fitted by a combination of a Gaussian and a Lorentzian, where the Lorentzian fraction A_f in Figure 3b reflects the fraction of mobile Li-ions. At 278 K, all Li-ions have a jump frequency that exceeds the static line width, reflected by the fact that the resonance can be fitted by a single narrow Lorentzian.

To quantitatively determine the Li-ion jump frequencies, temperature-dependent ^{7}Li static spin−lattice relaxation (SLR) rates in the laboratory frame $(1/T_1)$, and in the rotating frame, $(1/T_{1\rho})$ are measured, the results of which are shown in Figure 3c. The SLR rates, $1/T_1$ and $1/T_{1\rho}$, are directly related to the spectral density functions of the Li-ion jumping processes.[32] The temperature dependence of the SLR rate in the laboratory frame, $1/T_1$, can therefore be used to quantify the Li-ion jump frequency and the corresponding activation energy,[29,31,49,50] whereas the SLR rate in the rotating frame can be used to probe ionic motion taking place at a longer time scales.[29,31,49,50] When $1/T_{1(\rho)}$ reaches a maximum as a function of temperature, the hopping frequency $1/\tau$ is on the order of the Larmor frequency (ω_0) or lock frequency (ω_1), where τ equals the correlation time between hops.[29,31,49,50] Because the Larmor frequency is 155.506 MHz and the lock frequencies are in the kilohertz range, these SLR experiments are sensitive to Li-ion motion covering many orders of magnitude.

Starting with the SLR experiments in the laboratory frame, the condition at the maximum SLR $1/T_1$ rate versus temperature, occurring at 345 K in Figure 3c, is $\tau\omega_0 \approx 1$.[29,31,32,49,51] With a Larmor frequency of $\omega_0/(2\pi) = 155.506$ MHz, this results in a Li-ion jump frequency of $(9.8 \pm 0.1) \times 10^8$ s^{-1} at 345 K. Assuming a 3D diffusion process, in the high temperature limit, $\tau\omega_0 \ll 1$, the SLR rates are proportional to the Li-ion residence time τ, and in the low temperature limit, $\tau\omega_0 \gg 1$, the SLR rates are proportional to $\tau^{-1}\omega_{0(\rho)}^{-\beta}$ (with $1 < \beta \leq 2$). In particular, the $1/T_1$ rate appears to be asymmetric, here quantified by $\beta = 1.31$, similar to what was observed for Li_6PS_5Br.[20] This is most likely the result of Li-ion diffusional processes taking place at different length scales, as appears to be

DOI: 10.1021/jacs.6b05066
J. Am. Chem. Soc. 2016, 138, 11192−11201

the case in Li_6PS_5Cl, illustrated by the different transition types and transition rates predicted by the MD simulations. The asymmetry of the SLR $1/T_1$ rate indicates that the low temperature flank represents the short-range motional process whereas the high temperature flank most likely represents a longer range Li-ion diffusion process.[32,52] Assuming an Arrhenius behavior for the Li-ion residence time, $\tau = \tau_0 \exp(-E_a/(k_B T))$, the SLR rates in Figure 3c yield activation energies of 0.09 ± 0.02 and 0.29 ± 0.01 eV, respectively for the local Li-ion and long-range Li-ion diffusion processes, respectively. Given the activation energy for the long-range Li-ion diffusion, its jump frequency can be quantified to be $1/\tau = 2.0 \times 10^{13}$ Hz $\exp[-0.295\ \text{eV}/(k_B T)]$. At the onset temperature of the motional narrowing, 153 K, this results in a jump rate of 3.8 kHz, which is on the order of 5 kHz consistently explaining the motional narrowing observed in Figure 3a.

Comparison with the MD simulations indicates that the low temperature flank of the NMR SLR $1/T_1$ rate (characterized by an activation energy of 0.09 ± 0.02 eV) represents a combination of the two short-range, local Li-ion motional processes, the back-and-forth and intracage transitions, predicted to have an activation energy between 0.10 and 0.17 eV. The high temperature flank (0.29 ± 0.01 eV) represents the long-range intercage transitions, predicted to have an activation energy between 0.23 ± 0.02 and 0.25 ± 0.01 eV, which are responsible for the macroscopic diffusion. Consistently, the jump frequency based on the NMR SLR $1/T_1$ rate, approximately 1×10^{10} Hz at 450 K and 7×10^{10} Hz at 600 K, using the derived temperature dependent long-range transition frequency $1/\tau = 2.0 \times 10^{13}$ Hz $\exp[-0.295\ \text{eV}/(k_B T)]$, is comparable to that predicted by the MD simulations for the intercage transitions, see Table S2 in the Supporting Information.

In the rotating frame, the maximum $1/T_{1\rho}$ relaxation rate as a function of temperature, shown in Figure 3c, satisfies the condition $\tau_{1\rho}\omega_{\text{lock}} \approx 0.5$,[16−18,32] yielding jump rates of $(1.38 \pm 0.02) \times 10^5\ s^{-1}$ (at 200 K), $(5.3 \pm 0.1) \times 10^5\ s^{-1}$ (at 215 K), and $(1.06 \pm 0.02) \times 10^6\ s^{-1}$ (at 220 K) for the lock frequencies of 11, 42, and 84 kHz, respectively. At the high temperature flank, the $1/T_{1\rho}$ relaxation rates in Li_6PS_5Cl with the different lock frequencies yield similar activation energies compared with the activation energy of the $1/T_1$ relaxation rate, albeit slightly smaller, see Table S3 in the Supporting Information. Taking into account the activation energy of 0.29 eV, the jump frequency based on the $1/T_1$ relaxation, $9.8 \times 10^8\ s^{-1}$ at 345 K, results in $7.4 \times 10^5\ s^{-1}$ at 200 K. This value is comparable to the jump frequency derived from the $1/T_{1\rho}$ relaxation rate at the 11 kHz lock frequency ($1.38 \times 10^5\ s^{-1}$ at 200 K). This suggests that the $1/T_{1\rho}$ relaxation rate is due to a few intercage transitions, and apparently this extended diffusion range results in a lower transition barrier. Given the small particle size of the present Li_6PS_5Cl material, having an average particle size of 30 nm, the extended Li-ion range probed by the NMR SLR experiments in the rotating frame may be influenced by the Li_6PS_5Cl−Li_6PS_5Cl grain boundaries as discussed in the next paragraphs, suggesting that the grain boundaries have a lower activation energy for Li-ion diffusion.

Similar to the jump rates predicted by the MD simulations, the jump rates measured by the NMR SLR experiments can be used to determine the corresponding self-diffusion coefficients and conductivities, using a combination of the Einstein−Smoluchowski and the Nernst−Einstein relations, the results of which are shown in Figure 5 and reported in Table S3 of the Supporting Information.

Li-ion Exchange between Li_2S and Li_6PS_5Cl. The ^7Li NMR spin−lattice relaxation (SLR) experiments, shown in Figure 3, probe the bulk Li-ion mobility in the Li_6PS_5Cl electrolyte. In addition to bulk conductivity, a critical transport process in a solid-state cell is that between the solid electrolyte and solid electrode phases, the charge transfer reaction, in many cases suggested to be the bottleneck for the power density of all-solid-state batteries.[6,10,53] The difference in line width or in chemical shift allows NMR to probe the exchange of diffusing species between different chemical environments[54] enabling direct measurement of the equilibrium Li-ion exchange between different phases. This has been demonstrated by previous work where ^7Li exchange NMR was used to probe the spontaneous equilibrium exchange of Li-ions between two different solid electrode phases (Li-rich and Li-poor phases in anatase Li_xTiO_2)[35] and between the solid electrode phase and a liquid electrolyte phase (anatase $Li_{0.5}TiO_2$ and $LiPF_6$ in an EC/DMC solvent).[36] This extends the Li-ion diffusion time scale that can be probed with NMR from microseconds (with spin-relaxation experiments) up to seconds (with exchange NMR), depending on the material NMR characteristics.

In the present work, a similar approach is applied for a mixture of the argyrodite Li_6PS_5Cl electrolyte with the Li_2S positive electrode having particle sizes of 7 and 32 nm, respectively, as determined from Rietveld refinement of the XRD patterns. The static ^7Li NMR spectrum of the Li_6PS_5Cl−Li_2S mixture, Figure 4a, presents a clear difference in line width.

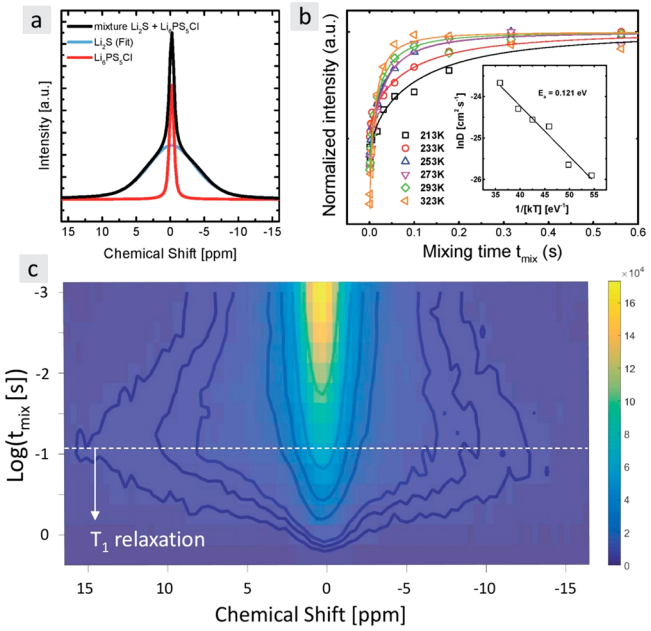

Figure 4. (a) The static ^7Li NMR spectrum of the electrode−solid electrolyte Li_2S−Li_6PS_5Cl mixture. (b) Normalized intensity of the static Li_2S ^7Li NMR spectrum, T_1 corrected, as a function of mixing time at different temperatures. The inset shows the temperature dependence of the diffusion parameter D, derived from the fits representing the diffusion model, see text. An Arrhenius law is used to fit the activation energy, E_a, representing the diffusion process over the boundary between the Li_6PS_5Cl solid electrolyte and the Li_2S phases. (c) One-dimensional ^7Li−^7Li NMR exchange experiment probing the Li-ion transport from the electrolyte Li_6PS_5Cl phase to the electrode Li_2S phase at room temperature.

DOI: 10.1021/jacs.6b05066
J. Am. Chem. Soc. 2016, 138, 11192−11201

The Li_6PS_5Cl resonance is significantly narrower, a consequence of the Li-ion induced motional narrowing as demonstrated in Figure 3a, whereas the much smaller mobility in the Li_2S positive electrode results in a broad resonance. This provides the necessary contrast for NMR exchange experiments, where the broad Li_2S resonance is filtered out by an echo experiment as described in the Experimental Section. The result of the 1D NMR ^{7}Li exchange experiment at room temperature is shown in Figure 4c. After filtering out the Li_2S resonance, the transfer of the magnetization, carried by the diffusing Li-ions, from the Li_6PS_5Cl solid electrolyte to the Li_2S phase is monitored as a function of mixing time, t_{mix}. At $t_{mix} = 0$, the top of the 2D plot, the narrow resonance originates solely from the Li-ions in the Li_6PS_5Cl solid electrolyte. With increasing mixing time, going down in Figure 4c, the narrow Li_6PS_5Cl NMR signal reduces in intensity because the Li-ions diffuse from the Li_6PS_5Cl phase toward the Li_2S phase. Thereby magnetization is transferred to the Li_2S phase causing a broad resonance, representing Li-ions in Li_2S, to appear with increasing mixing time t_{mix} as shown in Figure 4c. Thereby this experiment directly probes the spontaneous exchange of Li-ions, that is, the exchange current between the solid electrolyte and solid electrode phases, a direct measure for the kinetics of the charge transfer process. When the mixing time exceeds approximately 200 ms, the T_1 SLR of the Li_6PS_5Cl material causes the total magnetization to disappear, making it impossible to evaluate the exchange beyond this time scale. The 1D ^{7}Li NMR exchange experiment is performed at various temperatures and the resulting increase in the ^{7}Li signal of the Li_2S phase due to the Li-ion diffusion is shown in Figure 4b. To quantify the exchange between the Li_6PS_5Cl and Li_2S phases, the emerging Li_2S signal due to the magnetization transfer carried by the Li-ions is fitted with a diffusion model. Assuming that the spontaneous equilibrium exchange between the electrolyte and electrode phases can be described by an effective diffusion coefficient the solution to Fick's law for diffusion is determined, $\frac{\partial m(\vec{r},t)}{\partial t} = \vec{\nabla}\cdot\{D(\vec{r})m(\vec{r},t)\}$, where $m(\vec{r},t)$ is the magnetization of Li at position $\vec{r}$ and t and D is the Li-ion self-diffusion coefficient. According to the mathematical description of the model for spin-diffusion, elucidated in detail by Schmidt-Rohr and co-workers,[55] the rate of demagnetization of Li-ions in the solid electrolyte material is determined to be equal to the difference between the initial magnetization and the rate of magnetization in the electrode particles. Assuming a cubic shaped Li_6PS_5Cl solid electrolyte phase embedded in an infinite Li_2S phase, this results in the following analytical expression for the rate of demagnetization from the Li_6PS_5Cl electrolyte into the Li_2S electrode particles as[35]

$$m(t_{mix}) = \left\{ \frac{m_0}{2}\sqrt{4Dt_{mix}}\left[\text{ierfc}\left(\frac{d}{\sqrt{4Dt_{mix}}}\right) + \text{ierfc}\left(\frac{-d}{\sqrt{4Dt_{mix}}}\right) - \frac{2}{\sqrt{\pi}}\right]\right\}^3$$

where $\text{ierfc}(x) = 1/\sqrt{\pi}\,\exp(-x^2) - x(1 - \text{erf}(x))$ and d is the Li diffusion distance from the Li_6PS_5Cl particle to the Li_2S. For simplicity, it is assumed that diffusion occurs from the center of a Li_6PS_5Cl solid electrolyte particle to the center of the Li_2S electrode particle, which have individual particle sizes of 7 and 32 nm, respectively. Because of the larger Li_2S crystallite size and much smaller conductivity,[56,57] the assumption of an infinite Li_2S phase appears to be appropriate. Thus, the average diffusion distance is assumed to be the distance between the centers of the Li_6PS_5Cl and Li_2S grains, d = 20 nm. The fitted results of the normalized intensity of the upcoming Li_2S resonance as a function of mixing time for different temperatures are shown in Figure 4b. The inset of Figure 4b shows the resulting self-diffusion coefficient (D) as a function of temperature for Li-ion transfer over the electrolyte−electrode interface and the corresponding activation energy. It should be realized that the resulting diffusion coefficient is directly correlated to the lithium diffusion distance d, and the assumption that the Li-diffusion occurs from the center of a Li_6PS_5Cl particle to the center of the Li_2S particle is most likely an overestimation due to the poor conductivity of the Li_2S grains, thereby leading to an overestimation of the diffusion coefficient. The resulting self-diffusion coefficient for the Li_6PS_5Cl−Li_2S exchange is approximately 1×10^{-11} cm^2/s at room temperature, many orders of magnitude smaller than the Li_6PS_5Cl bulk diffusion coefficient resulting from the NMR SLR experiments, shown in Table S3 in the Supporting Information, and predicted by the MD simulations, shown in Table S2 in the Supporting Information. The unique ability of the exchange NMR to distinguish the transport over the Li_6PS_5Cl−Li_2S interface region indicates that crossing this interface presents a major bottleneck for Li-ion transport in the all-solid-state battery, compared with the transport through the Li_6PS_5Cl electrolyte. Surprisingly, the activation energy for the exchange is relatively small, 0.12 ± 0.01 eV, compared with that of the bulk diffusion, 0.29 ± 0.01 eV, as determined by the T_1 NMR SLR experiments. This suggests that Li-ion transport over the Li_6PS_5Cl−Li_2S interface is facile. However, the small diffusion coefficient implies that the equilibrium exchange current density is small. A rationale for that would be a small interfacial area between the electrolyte and electrode phases limiting the Li-ion transport over the Li_6PS_5Cl−Li_2S interface. This suggests that the creation of larger electrolyte−electrode interfacial areas, having intimate contact, is essential for the all-solid-state battery performance, for instance, as attempted with wetting agents.[3]

The conductivity results from the MD calculations the ^{7}Li NMR SLR experiments, the impedance spectroscopy, and the NMR exchange experiments are compared in Figure 5. This covers Li-ion transport over an extremely wide time-scale, from 10^{-12} s, representing intercage transitions, up to approximately 0.1 s, representing the exchange between the Li_6PS_5Cl electrolyte and Li_2S electrode. Fitting the conductivities derived from the ^{7}Li NMR SLR experiments with an Arrhenius law results in an activation energy of 0.33 ± 0.01 eV for the bulk Li-ion conductivity in Li_6PS_5Cl, slightly larger than the activation energies from the NMR SLR experiment itself. The difference is most likely the consequence of calculating the conductivity from the $R_{T1\rho}(1/T_{1\rho})$ experiments assuming a single intercage transition, whereas these experiments most likely probe multiple intercage transitions as discussed. This simplifying assumption is necessary because the diffusion distance during the $R_{T1\rho}$ experiments cannot be unambiguously determined. This effectively underestimates the conductivity resulting from the $R_{T1\rho}$ experiments, explaining the slightly larger activation energy in Figure 5 compared with that based on the NMR SLR experiments (see Table S3 in the Supporting Information). The bulk conductivities of Li_6PS_5Cl predicted by the MD simulations are in good agreement with those extrapolated

DOI: 10.1021/jacs.6b05066
J. Am. Chem. Soc. 2016, 138, 11192−11201

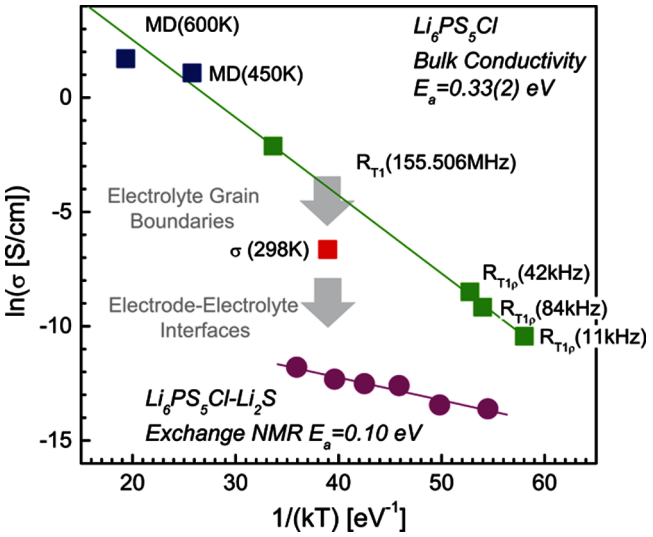

Figure 5. Li-ion conductivity in Li_6PS_5Cl deduced from the DFT MD simulations, ^{7}Li solid-state NMR SLR experiments, 1D exchange experiments between the Li_2S electrode and Li_6PS_5Cl solid electrolyte, and the room temperature impedance measurements.

from the NMR SLR results. Frequently MD simulations are based on simplified force field potentials, allowing larger diffusion times to be simulated in larger super cells, or the kinetic predictions are based on static nudged elastic band calculations disregarding the kinetics of the lattice. The present results demonstrate that DFT based MD simulations can be used to predict the Li-ion kinetics for these fast ionic conductive materials resulting in good agreement with the NMR SLR experiments. This allows one to gain more insight in the diffusion mechanism at the atomic scale, which is valuable for the design of novel solid electrolyte materials.

The room-temperature conductivity determined by impedance spectroscopy, Figure 1b, is significantly smaller, compared to the bulk conductivity measured by the NMR SLR experiments. As discussed, the NMR SLR experiments probe up to a few Li-ion transitions whereas impedance spectroscopy probes transport over a longer length scale, in the order of tens of nanometers typically. For the present nanostructured electrolyte material this suggests that impedance spectroscopy probes a mixture of the Li_6PS_5Cl bulk conductivity and the Li_6PS_5Cl–Li_6PS_5Cl grain boundaries. Therefore, the smaller conductivity by impedance spectroscopy compared with the NMR SLR experiments may indicate that grain boundaries lower the conductivity significantly. The present conductivity, measured by impedance spectroscopy, is comparable to that reported in literature[16,51,54−57] however the activation energy based on the NMR SLR experiments is relatively large compared to that measured with impedance spectroscopy by Rao et al., the latter reporting values as low as 0.11 and 0.16 eV for Li_6PS_5Cl.[25,28] Given the similar room temperature conductivity, and similarity in refined structure, it is unlikely that this is the consequence of a difference in the detailed structure and morphology of the presently prepared Li_6PS_5Cl material. Assuming that impedance spectroscopy probes both the bulk and grain boundary Li-ion diffusion, this suggests that the activation energy for grain boundary diffusion is smaller than that for the bulk diffusion. This is in line with the NMR SLR experiments in the rotating frame, probing longer range diffusion compared with the NMR SLR experiments in the laboratory frame, resulting in a slightly lower activation energy (see Table S3 in the Supporting Information). The smaller conductivity from impedance spectroscopy compared with the bulk conductivity probed by the NMR experiments may be explained by a small amount of grain boundary areas allowing facile Li-ion transport, similar to what was suggested for the electrolyte–electrode interface.

The NMR exchange experiments make it possible to characterize the equilibrium exchange of Li-ions over the Li_6PS_5Cl–Li_2S interface. Comparing these results with the bulk and impedance conductivity seen in Figure 5 suggests that the Li_6PS_5Cl grain boundaries limit the conductivity of the electrolyte and that the Li-ion transport over the Li_6PS_5Cl–Li_2S interface poses an even larger constraint for the charge transport between the electrolyte and electrode phases. This implies that the Li_6PS_5Cl–Li_2S interface is the dominant factor responsible for the restricted power performance of the present all-solid-state battery. The Li_6PS_5Cl–Li_6PS_5Cl and Li_6PS_5Cl–Li_2S interfaces can be anticipated to be relatively well connected with respect to charge transport compared with other solid electrolyte–electrode combinations, given the similar structure and low melting temperatures of Li_6PS_5Cl and Li_2S. Thus, the present results suggest that also for other solid electrolyte–electrode combinations the solid-electrolyte interfaces should be considered as the major bottleneck for charge transport in all-solid-state batteries. Interface design therefore should be considered one of the main directions to improve solid-state battery performance. The impedance spectroscopy results in Figure S2 in the Supporting Information shows that the degrading cycling performance goes along with an apparent increase in interfacial resistance. To establish the influence of the transport over the Li_6PS_5Cl–Li_2S interface, a next challenge will be to use the present NMR exchange experiments to characterize the Li-ion transport as a function of interface preparation procedures and as a function of battery cycling.

CONCLUSIONS

The bulk conductivity in argyrodite Li_6PS_5Cl is investigated by a combination of ^{7}Li NMR experiments and DFT based MD simulations. This reveals two clearly distinguishable Li-ion motional processes: (1) local transitions within the cage-like structure formed by Li-ion positions around the S or Cl atom and (2) intercage transitions, which are the limiting step for the macroscopic diffusion of Li-ions in the crystalline bulk Li_6PS_5Cl structure. Good agreement is established between the bulk conductivity probed by the NMR experiments and predictions by the DFT MD simulations. Comparison with the macroscopic conductivity measured with impedance spectroscopy suggests a significant influence of Li_6PS_5Cl–Li_6PS_5Cl grain boundaries on the conductivity of the electrolyte. However, using exchange NMR, the electrolyte–electrode Li_6PS_5Cl–Li_2S interface is found to be the major hurdle for Li-ion transport in all-solid-state batteries, limiting the power performance. Thereby, exchange NMR is demonstrated to be a valuable tool in all-solid-state battery research making it possible to unravel the different diffusional processes and to characterize the bottlenecks for Li-ion transport, one of the major challenges in all-solid-state batteries.

DOI: 10.1021/jacs.6b05066
J. Am. Chem. Soc. 2016, 138, 11192−11201

■ ASSOCIATED CONTENT

Supporting Information

The Supporting Information is available free of charge on the ACS Publications website at DOI: 10.1021/jacs.6b05066.

Cyclic voltammograms, electrochemical impedance spectra, jump frequencies, diffusion coefficients, conductivities, and activation energies from MD simulations and ^{7}Li NMR SLR experiments (PDF)

■ AUTHOR INFORMATION

Corresponding Author

*m.wagemaker@tudelft.nl

Notes

The authors declare no competing financial interest.

■ ACKNOWLEDGMENTS

The research leading to these results has received funding from the European Research Council under the European Union's Seventh Framework Programme (FP/2007-2013)/ERC Grant Agreement No. 307161 to M.W. Support from the Dutch organization of scientific research (NWO) for the solid-state NMR facility for advanced materials science in Nijmegen is gratefully acknowledged. The technical assistance of Hans Janssen, Gerrit Janssen, and Jan Schoonbrood is gratefully acknowledged. The solid-state NMR facility for advanced material science at the Radboud University is greatly acknowledged for supporting this research.

■ REFERENCES

(1) Etacheri, V.; Marom, R.; Elazari, R.; Salitra, G.; Aurbach, D. *Energy Environ. Sci.* **2011**, *4*, 3243.
(2) Minami, T.; Tatsumisago, M.; Wakihara, M.; Iwakura, C.; Kohjiya, S.; Tanaka, I. In *Solid State Ionics for Batteries*; Minami, T., Tatsumisago, M., Eds.; Springer Science & Business Media: Tokyo, 2006.
(3) Kim, J. G.; Son, B.; Mukherjee, S.; Schuppert, N.; Bates, A.; Kwon, O.; Choi, M. J.; Chung, H. Y.; Park, S. *J. Power Sources* **2015**, *282*, 299.
(4) Fergus, J. W. *J. Power Sources* **2010**, *195*, 4554.
(5) Tatsumisago, M.; Nagao, M.; Hayashi, A. *J. Asian Ceramic. Soc.* **2013**, *1*, 17.
(6) Takada, K. *Acta Mater.* **2013**, *61*, 759.
(7) Park, M.; Zhang, X.; Chung, M.; Less, G. B.; Sastry, A. M. *J. Power Sources* **2010**, *195*, 7904.
(8) Tatsumisago, M.; Hayashi, A. *Int. J. Appl. Glass Sci.* **2014**, *5*, 226.
(9) Knauth, P. *Solid State Ionics* **2009**, *180*, 911.
(10) Cao, C.; Li, Z.-B.; Wang, X.-L.; Zhao, X.-B.; Han, W.-Q. *Front. Energy Res.* **2014**, *2*, 25.
(11) Takada, K. *Langmuir* **2013**, *29*, 7538.
(12) Takada, K.; Ohta, N.; Zhang, L.; Xu, X.; Hang, B. T.; Ohnishi, T.; Osada, M.; Sasaki, T. *Solid State Ionics* **2012**, *225*, 594.
(13) Mizuno, F.; Hayashi, A.; Tadanaga, K.; Tatsumisago, M. *Adv. Mater.* **2005**, *17*, 918.
(14) Kamaya, N.; Homma, K.; Yamakawa, Y.; Hirayama, M.; Kanno, R.; Yonemura, M.; Kamiyama, T.; Kato, Y.; Hama, S.; Kawamoto, K.; Mitsui, A. *Nat. Mater.* **2011**, *10*, 682.
(15) Deiseroth, H.-J.; Kong, S.-T.; Eckert, H.; Vannahme, J.; Reiner, C.; Zaiß, T.; Schlosser, M. *Angew. Chem., Int. Ed.* **2008**, *47*, 755.
(16) Thangadurai, V.; Narayanan, S.; Pinzaru, D. *Chem. Soc. Rev.* **2014**, *43*, 4714.
(17) Aono, H.; Sugimoto, E.; Sadaoka, Y.; Imanaka, N.; Adachi, G. y. *J. Electrochem. Soc.* **1990**, *137*, 1023.
(18) Seino, Y.; Ota, T.; Takada, K.; Hayashi, A.; Tatsumisago, M. *Energy Environ. Sci.* **2014**, *7*, 627.
(19) Chen, H. M.; Maohua, C.; Adams, S. *Phys. Chem. Chem. Phys.* **2015**, *17*, 16494.
(20) Epp, V.; Gün, Ö.; Deiseroth, H.-J.; Wilkening, M. *J. Phys. Chem. Lett.* **2013**, *4*, 2118.
(21) Boulineau, S.; Courty, M.; Tarascon, J.-M.; Viallet, V. *Solid State Ionics* **2012**, *221*, 1.
(22) Boulineau, S.; Tarascon, J.-M.; Leriche, J.-B.; Viallet, V. *Solid State Ionics* **2013**, *242*, 45.
(23) Chen, M.; Adams, S. *J. Solid State Electrochem.* **2015**, *19*, 697.
(24) Rao, R. P.; Adams, S. *Phys. Status Solidi A* **2011**, *208*, 1804.
(25) Rao, R. P.; Sharma, N.; Peterson, V. K.; Adams, S. *Solid State Ionics* **2013**, *230*, 72.
(26) Pecher, O.; Kong, S. T.; Goebel, T.; Nickel, V.; Weichert, K.; Reiner, C.; Deiseroth, H. J.; Maier, J.; Haarmann, F.; Zahn, D. *Chem. - Eur. J.* **2010**, *16*, 8347.
(27) Deiseroth, H.-J.; Maier, J.; Weichert, K.; Nickel, V.; Kong, S.-T.; Reiner, C. *Z. Anorg. Allg. Chem.* **2011**, *637*, 1287.
(28) Rayavarapu, P.; Sharma, N.; Peterson, V.; Adams, S. *J. Solid State Electrochem.* **2012**, *16*, 1807.
(29) Epp, V.; Wilkening, M. In *Handbook of Solid State Batteries*, 2nd ed.; Dudney, N. J., West, W. C., Nanda, J., Eds.; World Scientific: Hong Kong, 2015; p 133.
(30) Kuhn, A.; Kunze, M.; Sreeraj, P.; Wiemhöfer, H.-D.; Thangadurai, V.; Wilkening, M.; Heitjans, P. *Solid State Nucl. Magn. Reson.* **2012**, *42*, 2.
(31) Wilkening, M.; Heitjans, P. *ChemPhysChem* **2012**, *13*, 53.
(32) *Diffusion in Condensed Matter: Methods, Materials, Models*, 2nd ed.; Heitjans, P.; Kärger, J., Eds.; Springer-Verlag: Berlin Heidelberg, 2005.
(33) Wohlmuth, D.; Epp, V.; Wilkening, M. *ChemPhysChem* **2015**, *16*, 2582.
(34) Breuer, S.; Prutsch, D.; Ma, Q.; Epp, V.; Preishuber-Pflügl, F.; Tietz, F.; Wilkening, M. *J. Mater. Chem. A* **2015**, *3*, 21343.
(35) Wagemaker, M.; Kentgens, A.; Mulder, F. *Nature* **2002**, *418*, 397.
(36) Ganapathy, S.; van Eck, E. R.; Kentgens, A. P.; Mulder, F. M.; Wagemaker, M. *Chem. - Eur. J.* **2011**, *17*, 14811.
(37) Kresse, G.; Hafner, J. *Phys. Rev. B: Condens. Matter Mater. Phys.* **1993**, *47*, 558.
(38) de Klerk, N. J.; Wagemaker, M. *Chem. Mater.* **2016**, *28*, 3122.
(39) Takeuchi, T.; Kageyama, H.; Nakanishi, K.; Tabuchi, M.; Sakaebe, H.; Ohta, T.; Senoh, H.; Sakai, T.; Tatsumi, K. *J. Electrochem. Soc.* **2010**, *157*, A1196.
(40) Takeuchi, T.; Sakaebe, H.; Kageyama, H.; Senoh, H.; Sakai, T.; Tatsumi, K. *J. Power Sources* **2010**, *195*, 2928.
(41) Hayashi, A.; Ohtsubo, R.; Tatsumisago, M. *Solid State Ionics* **2008**, *179*, 1702.
(42) Hayashi, A.; Ohtsubo, R.; Ohtomo, T.; Mizuno, F.; Tatsumisago, M. *J. Power Sources* **2008**, *183*, 422.
(43) Chen, M.; Rao, R. P.; Adams, S. *Solid State Ionics* **2014**, *262*, 183.
(44) Huang, B.; Yao, X.; Huang, Z.; Guan, Y.; Jin, Y.; Xu, X. *J. Power Sources* **2015**, *284*, 206.
(45) Friauf, R. J. *J. Appl. Phys.* **1962**, *33*, 494.
(46) Mehrer, H. *Diffusion in Solids: Fundamentals, Methods, Materials, Diffusion-Controlled Processes*; Springer Science & Business Media: Berlin, 2007; Vol. *155*.
(47) Vineyard, G. H. *J. Phys. Chem. Solids* **1957**, *3*, 121.
(48) Van der Ven, A.; Ceder, G.; Asta, M.; Tepesch, P. *Phys. Rev. B: Condens. Matter Mater. Phys.* **2001**, *64*, 184307.
(49) Kuhn, A.; Choi, J.-Y.; Robben, L.; Tietz, F.; Wilkening, M.; Heitjans, P. *Z. Phys. Chem.* **2012**, *226*, 525.
(50) Kuhn, A.; Narayanan, S.; Spencer, L.; Goward, G.; Thangadurai, V.; Wilkening, M. *Phys. Rev. B: Condens. Matter Mater. Phys.* **2011**, *83*, 094302.
(51) Bloembergen, N.; Purcell, E. M.; Pound, R. V. *Phys. Rev.* **1948**, *73*, 679.
(52) Epp, V.; Gun, O.; Deiseroth, H.-J.; Wilkening, M. *J. Phys. Chem. Lett.* **2013**, *4*, 2118.

DOI: 10.1021/jacs.6b05066
J. Am. Chem. Soc. 2016, 138, 11192−11201

(53) Minami, T.; Hayashi, A.; Tatsumisago, M. *Solid State Ionics* **2006**, *177*, 2715.
(54) Ernst, R. R.; Bodenhausen, G.; Wokaun, A. *Principles of Nuclear Magnetic Resonance in One and Two Dimensions*; Clarendon Press: Oxford, 1987; Vol. *14*.
(55) Spiess, H. W. *Multidimensional Solid-State NMR and Polymers*; Academic Press, New York, 1994.
(56) Mousa, M.; Oei, Y.; Richtering, H. *J. Phys. Colloq.* **1980**, *41*, C6.
(57) Yang, Y.; Zheng, G.; Misra, S.; Nelson, J.; Toney, M. F.; Cui, Y. *J. Am. Chem. Soc.* **2012**, *134*, 15387.

DOI: 10.1021/jacs.6b05066
J. Am. Chem. Soc. 2016, 138, 11192−11201